

Design improvement of thermal management for Li-ion battery energy storage systems

Pourya Ashkboos^{a,1}, Amin Yousefi^{a,1}, Ehsan Houshfar^{b,*}

^a Faculty of New Sciences and Technologies, University of Tehran, Tehran, Iran

^b School of Mechanical Engineering, College of Engineering, University of Tehran, P.O. Box 11155-4563, Tehran, Iran

ARTICLE INFO

Keywords:

Lithium-ion battery
Ribbed channel
Hydrothermal performance factor
Pumping power
Thermal management system

ABSTRACT

Thermal management of lithium-ion battery cells provides several advantages to reach high performance electric-vehicles and hybrid-electric-gadgets. Geometrical features and patterns of internal channels of liquid cooling plate (LCP) are key factors for the battery cell cooling efficiency. This paper concerns a new design of battery thermal management and the effect of ribbed channels with double inlets and outlets on the reduction of mass flowrate in the coolant channels of LCP, the hydrothermal performance factor of the battery, the friction coefficient, and the reduction of pumping power by utilizing comprehensive 3D simulations. The Conjugate Heat Transfer approach is employed for the fluid flow and the heat transfer calculations. To enhance the heat transfer surface and cooling efficiency, longitudinal ribs are considered in four different configurations inside the cooling channels. Furthermore, the effects of ribs on the aforementioned parameters in comparison with the non-rib channels are investigated. The results demonstrated that the optimized ribbed configuration increases the total amount of heat transfer by up to 68%, reduces the mass flowrate to 16%, and lowers the pumping power by 20% in comparison with rib-less channels. Meanwhile, the hydrothermal cooling performance factor of enhanced up to 58% and the maximum temperature approximately remains constant.

Introduction

Among all types of energy storage options, lithium-ion batteries (LIBs) play a significant role for electric vehicles (EVs) due to their merits of saving power and energy. Increasing generation of renewable-based electricity has also emphasized the importance of battery energy storage systems [1]. The efficient range for operating temperature of LIB is 20–40 °C and investigations clarified that in this range the battery has the best performance [2,3]. Furthermore, in high operating temperature conditions the maximum temperature of the battery rises rapidly [4] and may lead to the battery lifecycle reduction. Moreover, various configurations of Battery Thermal Management System (BTMS) induced different efficiency levels [5]. Consequently, design optimization and accurate simulation of battery thermal management (BTM) is inevitable and the development of the heat transfer and cooling performance of the battery is a significant matter as well as other devices. There are three major categories for investigations. Firstly, the analysis and simulation of unsteady battery current during charge/discharge and heat generation modes has monumental role in the subject. In addition, some

scholars focused on the geometrical aspects of the BTMS and others have studied the aspects of battery cooling medium, which can play an important role in controlling the battery temperature. Commonly the BTM are classified according to their mediums, including air-based medium, phase-change material (PCM), and liquid-based medium.

Yu et al. [6] designed a battery cooling system with two airflow channels and forced convection heat transfer for cooling the battery middle cells and the cooling channels. They investigated the BTM system using a comprehensive 3D numerical simulation and improved the maximum and uniformity of temperature within the battery. In a numerical study undertaken by Fan et al. [7], a commercial CFD code used to investigate the effect of air flowrate and spacing gap between neighboring cells on the maximum temperature of cells. They concluded that smaller gaps and higher flowrates lead to decrease of maximum cell temperature. Moreover, to improve temperature uniformity in the cells, the gap between adjacent cells should be moderate. The design optimization of BTMS is carried out by Chen et al. [8]. They studied the position of inlet and outlet of airflow for cooling a Li-ion battery and presented that the flow inlet and outlet position in the middle of the BTMS has the best performance. Cylindrical and flat-plate geometries

* Corresponding author at: Room 328, Mech. Eng. Dept. (Old Building), Campus 2, College of Engineering, University of Tehran, North Kargar St., Tehran, Iran.
E-mail address: houshfar@ut.ac.ir (E. Houshfar).

¹ P. Ashkboos and A. Yousefi contributed equally to this work as first authors.

Nomenclature			
BTM	Battery thermal management	Pr	Prandtl number
C-rate	Capacity rate	ΔP	Pressure drop of cooling channel (Pa)
EV	Electric vehicle	q_v	Volumetric heat generation (W m^{-3})
LCP	Liquid cooling plate	\dot{Q}	Volumetric flow rate ($\text{m}^3 \text{s}^{-1}$)
LFP	Lithium iron phosphate	R	Internal resistance of battery (Ω)
LIB	Lithium-ion battery	Re	Reynolds number
PCM	Phase change material	T_a	Ambient temperature ($^{\circ}\text{C}$)
P.P	Pumping power	T_c	Battery cell temperature ($^{\circ}\text{C}$)
SOC	State of charge	T_o	Outlet temperature of the coolant channel
c	Specific heat of battery ($\text{J kg}^{-1} ^{\circ}\text{C}^{-1}$)	T_b	Temperature of the main flow
c_{lcp}	Specific heat of liquid cooling plate ($\text{J kg}^{-1} ^{\circ}\text{C}^{-1}$)	T_{lcp}	Liquid cooling plate temperature ($^{\circ}\text{C}$)
c_N	Rated capacity of battery (Ah)	T_{max}	Maximum temperature of the battery ($^{\circ}\text{C}$)
c_w	Specific heat of water ($\text{J kg}^{-1} ^{\circ}\text{C}^{-1}$)	T_w	Temperature of liquid water ($^{\circ}\text{C}$)
D_H	Hydraulic diameter (m)	U	Current velocity (m s^{-1})
f	Friction factor	U_{ocv}	Open circuit voltage (V)
g	Gravitational acceleration (m s^{-2})	V_b	Battery cell volume (m^3)
k_{al}	Thermal conductivity of aluminum ($\text{W m}^{-1} ^{\circ}\text{C}^{-1}$)	W	Width of rib (mm)
h_f	Frictional head loss (m)	Greek letters	
h_j	Local head loss (m)	ξ	Coefficient of local resistance
h_w	Pump head (m)	ρ	Density of battery (kg m^{-3})
I	Operating current (A)	ρ_{lcp}	Density of liquid cooling plate (kg m^{-3})
L	Length of channel (m)	μ	Dynamic viscosity (Pa s)
Nu	Nusselt number (—)	η	Hydrothermal performance factor
P_w	Static pressure of water (Pa)	η_o	Ratio of power consumption

have been investigated with numerical and analytical models for an airflow medium by Xun et al. [9]. Their results revealed that the temperature behavior of the battery is independent to the airflow channel size and number of channels. Furthermore, the results demonstrated that although both cylindrical and flat plate geometries have the same effect in reducing the battery temperature, the cylindrical geometry is more cost-effective. Annular cooling duct geometry is addressed by Shah et al. [10] with air-cooling medium. The results demonstrated a promising thermal improvement of the battery cells and cooling system. Mohammadian and Zhang [11] studied a new BTM system with the pin-fin in the cooling channels and airflow as the medium. Three-dimensional investigation is carried out with different kinds of pin fins geometries, flow inlet velocities, and temperature for the battery cooling system. They concluded that utilizing pin fins have a promising development in the battery thermal uniformity and decreasing the battery temperature compared with the channels without pins. Furthermore, they studied the effect of pin fins structure with linearly increasing height along the cooling channel width and revealed better temperature uniformity and temperature decrease than the simple pin fins. They also observed that increasing the airflow inlet temperature leads to better temperature uniformity, and furthermore, airflow inlet velocity enhancement reduces the maximum temperature of the battery. The improvement of heat transfer by using snail entrance and cooled air is investigated by Durmus et al. [12]. They concluded the enhancement of the heat transfer albeit pressure drop increasing, however the heat transfer development is more effective.

Jiang et al. [13] designed a novel passive thermal management system with forced air-based and PCM to monitor the cell temperature and enhance heat transfer on the Li-ion battery pack utilizing ANSYS FLUENT simulation. Their results indicated that paraffin composite reduced the cells temperature and kept the maximum temperature difference in the battery module 1–2 $^{\circ}\text{C}$ lower, and baffles improved heat transfer efficiency by changing the direction of airflow. Fathabadi [14] designed a cooling management system with passive and active cooling parts. In the active part, airflow was utilized in the cooling ducts and the passive part included graphite composite as the PCM. The numerical

investigation of voltage and temperature of the battery clarified admissible improvement in the battery thermal performance. Chen et al. [15] performed a thorough review on PCMs based on the BTMS. They reported that almost all PCMs that have a solid–liquid phase have a low thermal conductivity, which makes it possible for heat to accumulate under difficult working conditions, and adding high-carbon materials will considerably increase the thermal conductivity. Moreover, hybrid BTMS, compared to single BTMS, cause the battery temperature to drop further and become more uniform. Thereby, hybrid systems are more appropriate for high-power batteries [16–19]. Safdari et al. [20] investigated a hybrid BTMS with active and passive cooling. They utilized three kinds of channel geometries with hexagonal, rectangular, and circular cross-sections and indicated that the circular geometry has the best efficiency. Furthermore, Investigation of different PCM as mediums for heat transfer is performed by Esen et al. [21–23]

Mohammadian et al. [24] investigated the effects of internal and external cooling methods on the cooling process of Li-ion batteries. They used liquid-based medium as the cooling fluid in their research and studied the temperature reduction as well as uniformity. Their results revealed that in the identical power consumption, the internal cooling system had advantages compared with the external cooling methods for the Li-ion battery. Jilte et al. [25] performed two methods for cooling BTMS in mini-channels. They utilized water and nanofluid as cooling mediums for the first cooling method. Furthermore, they reported effectiveness of using recirculated airflow for decreasing the battery temperature during the air conditioning process of the EVs. They revealed that, based on the atmospheric conditions, each method can be used to develop the cooling performance. To increase the heat transfer from the surface, Zhang et al. [26] suggested guide plates attached to S-shape liquid passage for cooling the high-charge element with high flux. Their numerical results indicated that for the S-shape cold-plate, the thermal efficiency is seven times higher than the linear cold-plate. Using heat pipes with the water-cooling BTM is studied by Rao et al. [27] for saving cost and energy. Based on their research, an experimental unsteady investigation is carried out to decrease the maximum battery temperature and results showed a promising improvement in BTM

Table 1
Battery cells Specifications.

Parameter	Value
Dimensions (mm)	$17 \times 79 \times 124$
Specific heat capacity ($\text{J kg}^{-1} \text{ } ^\circ\text{C}^{-1}$)	1305
Thermal conductivity ($\text{W m}^{-1} \text{ } ^\circ\text{C}^{-1}$)	2.6
Normal voltage (V)	3.2
Rated capacity (Ah)	8

performance by using the heat pipes. Optimization of BTM system is studied by Wiriyasart et al. [28]. They simulated nanofluid as the coolant medium in mini-channels and assessed the effects of mass flowrate and flow direction. The results revealed that utilizing nanofluid instead of water could improve thermal behavior of the battery cooling system while increasing the pressure drop of the channels. Lyu et al. [29] designed a novel BTMS which is combined with forced liquid-cooling arrangements. Their experimental data showed improvement of performance and temperature in comparison with the traditional BTMS. Furthermore, thermoelectric system is utilized for both heating and

cooling of the battery at different atmospheric conditions. The battery temperature uniformity is improved by design and optimization of a thermal management system for Li-ion battery by Cao et al. [30]. They showed a promising improvement in the performance and reduction in power consumption at the cooling flowrate of 40 L s^{-1} . Furthermore, in an investigation, Cao et al. [31] analyzed a hybrid BTMS utilizing water cooling mediums. They studied the effects of inlet mass flowrate and temperature on the performance of Li-ion battery. They represented that increasing the mass flowrate of the inlet flow leads to significant enhancement of the power consumption and the optimum temperature of inlet flow is $30 \text{ } ^\circ\text{C}$. Geometrical optimization of BTMS with mini-channels using genetic algorithm is performed by Liu et al. [32] using water as the fluid medium. They indicated that the tree-like geometry of the mini-channels develop the thermal performance in comparison with the straight channels. Neubauer discussed the BTMS as an alarming concern to control the battery temperature. They concluded that liquid-based system has advantages of heat extraction enhancement and life-time improvement. Sheng et al. [33] developed a novel coolant channel with liquid cooling plate (LCP) which had multi channels for the BTM,

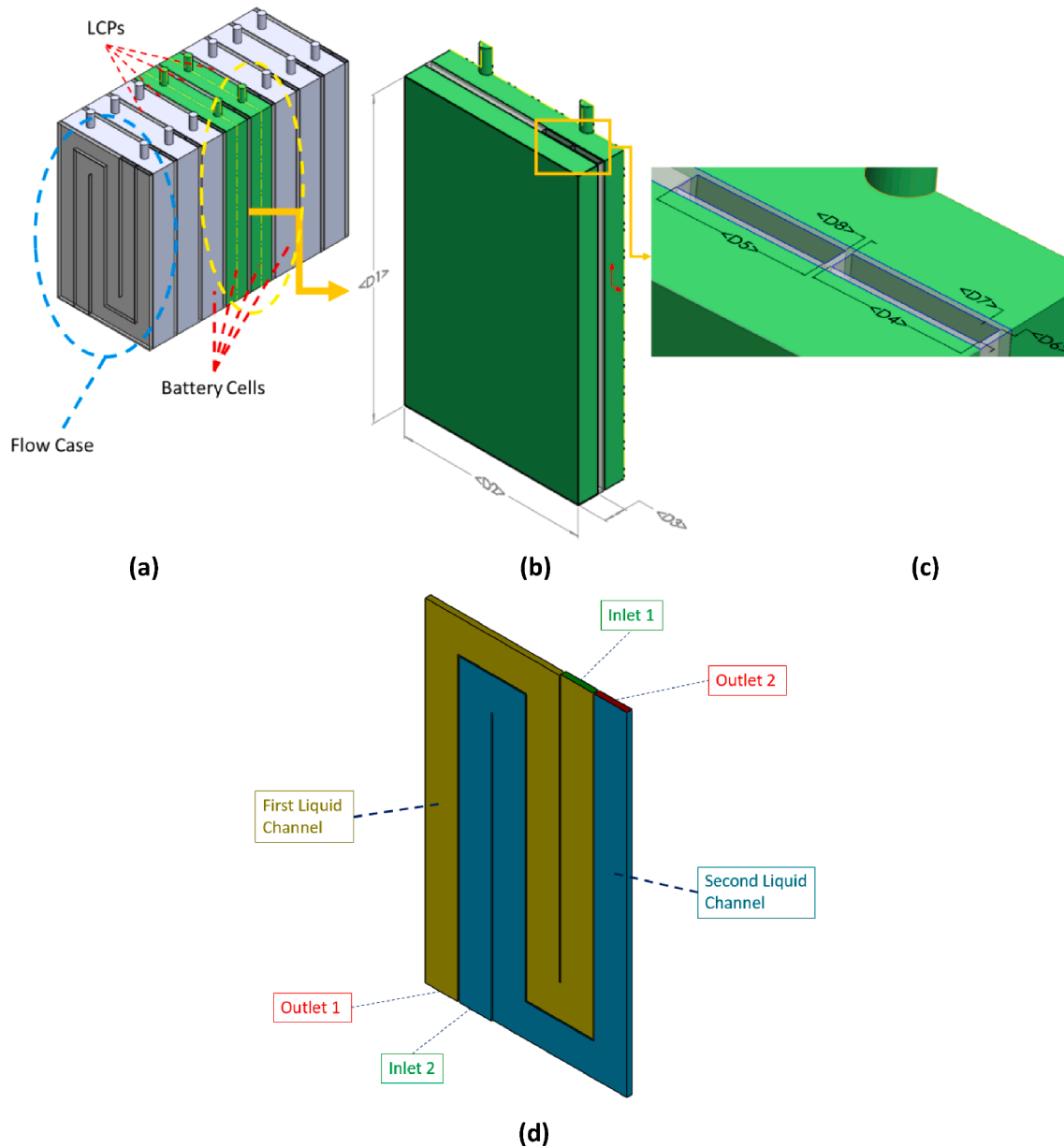


Fig. 1. BTMS geometry and flow paths: (a) Lithium-ion battery, (b) Simulation model, (c) Cooling channels, and (d) LCP.

Table 2

The simulation model and cooling ducts dimensions.

Dimension	D1	D2	D3	D4	D5	D6	D7	D8
Value (mm)	124	79	8.5	12	12	4	0.5	0.5

Table 3

Dimensions of LCP and material properties.

Contents	LCP	Fluid
Dimensions (mm)	3 × 179 × 124	N/A
Thermal conductivity (W m ⁻¹ °C ⁻¹)	202.4	0.6
Density (kg m ⁻³)	2719	1000
Specific heat (J kg ⁻¹ °C ⁻¹)	871	4200
Viscosity (kg m ⁻¹ s ⁻¹)	N/A	0.001003

and numerically investigated the effect of various parameters, including: the position of coolant channels in six different arrangements, the inlet mass flowrate, the width of coolant channels, and three different operating currents on the temperature distribution of the battery cells. Their results clarified that increasing the coolant mass flowrate lowers the temperature of battery cells. Furthermore, optimizing the width of coolant channels had a minor effect on the maximum temperature of the battery cells.

In view of all that has been mentioned so far, one may suppose that, in the existing surveys the impact of key parameters such as longitudinal ribs in liquid-based BTMS has not been comprehensively analyzed. This has considerable effect on the hydrothermal cooling performance of battery which can be used to optimize the Li-ion battery life cycle. To eliminate the existing gap, this paper examines the effects of longitudinal ribs on the thermal performance of liquid-based Li-ion battery and improves the design of these parameters. To decrease mass flowrate in the cooling paths, and increase the hydrothermal cooling performance factor of the battery, specific ribs were considered in the serpentine-shape channel of LCP with multi channels. The novelty of this work in comparison with the previous works is, therefore, a new design of BTM and development of the LCP heat transfer efficiency

Modeling and numerical methods

Battery model

In this work, a line of T-type battery model, that are connected in series with LCPs including double inlets and outlets, are considered for the investigation. Table 1 represents the battery cell specifications, including dimensions, thermal conductivity, and specific heat transfer coefficient. The anodes are made of iron lithium phosphate (LiFePO₄, LFP) which is the best active material for development of BTM [34]. The cathode material is graphite, and the electrolyte is made of a combination of dimethyl carbonate, ethylene carbonate, and ethyl methyl carbonate.

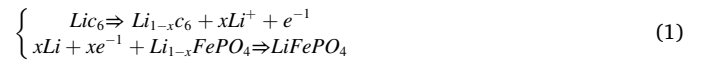
Fig. 1 (a) shows the geometry of the battery cells, LCPs, the flow case and the cooling paths which are attached to the battery cells. Due to the symmetry of the simulation model, for reduction of the computational costs, the simulation model can be considered as in Fig. 1 (b). The length, width, and half-thickness of the battery cells are indicated as D1, D2, and D3 in Fig. 1 (b), respectively. In Fig. 1 (c), D4 and D5 are widths of coolant channels, D6 is the flow duct height, D7 is the thickness of the LCP and D8 is the space between the two cooling ducts. Table 2 and 3 summarize the dimensions of the battery and the LCP.

Fig. 1 (d) shows the schematic of multi flow channels which are considered for the LCP. The position of inlets and outlets and the dimensions and shape of the channels in the LCP are chosen based on the superior case in the study of Sheng et al. [33] Two channels are considered with to fluid flow in opposite directions to improve the effectiveness of the cooling plates.

The parameters of the cooling water and the LCP are represented in Table 1, according to the reference case [33].

Governing equations

In a Li-ion battery, oxidization of lithium at the anode part leads to Li⁺ production, and the oxidization in the cathode part generates e⁻. Consequently, the chemical reactions in the battery are illustrated by Eq. (1).



The combination of the unsteady heat generation and transfer equations in the battery cell can be introduced by,

$$\rho c \frac{\partial T_b}{\partial t} = k \nabla^2 T_c + q_v \quad (2)$$

Where ρ is the cell density (kg m⁻³), c is the specific heat (J kg⁻¹ °C⁻¹), T_c is the cell temperature (°C), t is the time (s), k is the thermal conductivity (W m⁻¹ °C⁻¹), and q_v is the heat generation rate of cell (W m⁻³).

In addition, the equilibrium equation between the conduction and convection heat transfer for the adjacent surfaces leads to convection boundary condition, which is demonstrated by,

$$-k_{al}\Delta T = h(T_c - T_a) \quad (3)$$

Where k_{al} is the thermal conductivity of aluminum, h is the convection heat transfer coefficient of the surface (W m⁻² °C⁻¹), and T_a is the ambient temperature (°C).

The conservation equations for the mass, momentum, and energy of the cooling medium in the channels of the LCP are as follows,

$$\begin{cases} \frac{\partial \rho_w}{\partial t} + \nabla(\rho_w U) = 0 \\ \frac{\partial}{\partial t}(\rho_w U) + \nabla(\rho_w U U) = -\nabla P_w \\ \frac{\partial}{\partial t}(\rho_w c_w T_w) + \nabla(\rho_w c_w U T_w) = -\nabla(k_w \nabla T_w) = -\nabla(k_w \nabla T_w) \end{cases} \quad (4)$$

Where ρ_w , U , P_w , c_w , T_w , and k_w are the cooling medium density (kg m⁻³), the velocity of liquid (m s⁻¹), the static pressure (Pa), the specific heat coefficient (J kg⁻¹ °C⁻¹), the temperature (°C), and the thermal conductivity (W m⁻¹ °C⁻¹), respectively.

Non-dimensional equations and parameters

To increase the heat transfer of the battery cells, various types of ribs are created in the coolant channels. For measurement of the main parameters, the following steps have been followed. Eq. (5) is used to calculate the convection heat transfer coefficient on the battery surface.

$$h = \frac{q_w}{T_b - T_{sw}} \quad (5)$$

Where q_w , T_{sw} , and T_b denote the vane heat flux, the temperature of the battery surface, and the temperature of the main flow, respectively.

The Nusselt number is obtained from the following equation:

$$Nu = \frac{q_w}{T_{sw} - T_o} \cdot \frac{D_H}{k_w} \quad (6)$$

Where q_w represents the heat flux in the cooling paths, T_o is the temperature at the outlet of the coolant channels, T_{sw} is the average temperature of the battery surface and k_w represents the thermal conduction coefficient of water at the temperature of T_{sw} . Moreover, D_H is the hydraulic diameter of the coolant paths.

The hydrothermal cooling performance factor of the battery is then calculated using the equation proposed by Rehman et al. [35]:

Table 4

Heat generation coefficients for Eq. (14).

	G_0	G_1	G_2	G_3	G_4	G_5	G_6	R-squared
9C-rate	319.9	-2719.0	15148.5	-43018.3	63645.5	-46817.9	13257.5	0.999

$$\eta = \frac{\left(\frac{Nu}{Nu_0}\right)}{\left(\frac{f}{f_0}\right)^{\frac{1}{3}}} \quad (7)$$

Where Nu and Nu_0 represent the average Nusselt number in the ribbed and rib-less channels, respectively.

The friction factor (f) for the fluid flow depends on the state of the flow (laminar or turbulent) and is defined as follows:

$$f = \begin{cases} \frac{64}{Re} \text{LaminarFlow} \\ 2\rho \frac{\Delta P}{l} \times \left(\frac{A_c}{\dot{m}}\right)^2 \times D_H \text{TurbulentFlow} \end{cases} \quad (8)$$

where ρ represents the fluid density, ΔP denotes the pressure drop across the cooling channels, l represents the length of the coolant paths where ΔP is measured, A_c is the cross-section area, \dot{m} represents the mass flowrate and D_H denotes the hydraulic diameter of the coolant channels.

In Eq. (7), f_0 is friction factor in the rib-less channels. The values of Nu , Nu_0 , f , and f_0 are measured for the two channels separately and used for calculating the performance factor of the battery cell.

The required pumping power ($P.P$) for a volumetric flow rate of \dot{Q} through the pressure drop (ΔP) is estimated from:

$$P.P = \dot{Q} \times \Delta P = U_m \times A_c \times \Delta P \quad (9)$$

where A_c is the cross-sectional area and U_m is the maximum flow velocity at inlet of the channel.

Valiantzas [36] showed that the frictional head loss of incompressible viscous flow through a steadily rough channel could be obtained from:

$$h_f = f \frac{l}{D_h} \frac{u^2}{2g} \quad (10)$$

Where h_f is frictional head loss, f is friction factor which depends on the Reynolds number and calculated based on Eq. (8) and Moody

diagram. Moreover, the local resistance loss of the cooling duct is given by:

$$h_j = \xi \frac{u^2}{2g} \quad (11)$$

Where ξ is the local resistance coefficient, and when the fluid flows turn 90° inside the coolant channel, its value considered as 1.5 [33].

The power consumption ratio gives a measure of head loss in a channel to the total head of the pump and is defined as,

$$\eta_0 = \frac{\sum h_j + \sum h_f}{h_w} \times 100 \quad (12)$$

Where h_w is the total pump head. It should be highlighted that in general, a pump head of 10 m is considered for a BTMS [33].

Source heat generation equation for the battery cell

The unsteady heat generation in a battery is one of the significant factors which affect the battery temperature. It changes with various factors such as state of charge (SOC) [37], operating current, and life-cycle of the battery. The operating current is considered constant in this paper, therefore, the unsteady heat generation could be stated as [38]:

$$q_v = \frac{1}{V_b} \left(I^2 R - I T_b \frac{dU_{ocv}}{dT_b} \right) \quad (13)$$

Where V_b is the volume of the battery cell (m^3), R is the internal resistance (Ω), I is the operating current (A), U_{ocv} is the operating voltage (V), and $\frac{dU_{ocv}}{dT_b}$ is the coefficient of entropy ($V K^{-1}$).

The heat generation in the battery at $30^\circ C$ and for the operating current of 9C could be calculated by curve fitting of Eq. (13) as,

$$q_v (kWm^{-3}) = G_0 + G_1 S + G_2 S^2 + G_3 S^3 + G_4 S^4 + G_5 S^5 + G_6 S^6 \quad (14)$$

In Eq. (14), the coefficients G_0 to G_6 are represented in Table 1. S is the SOC and for the constant operating current can be calculated by,

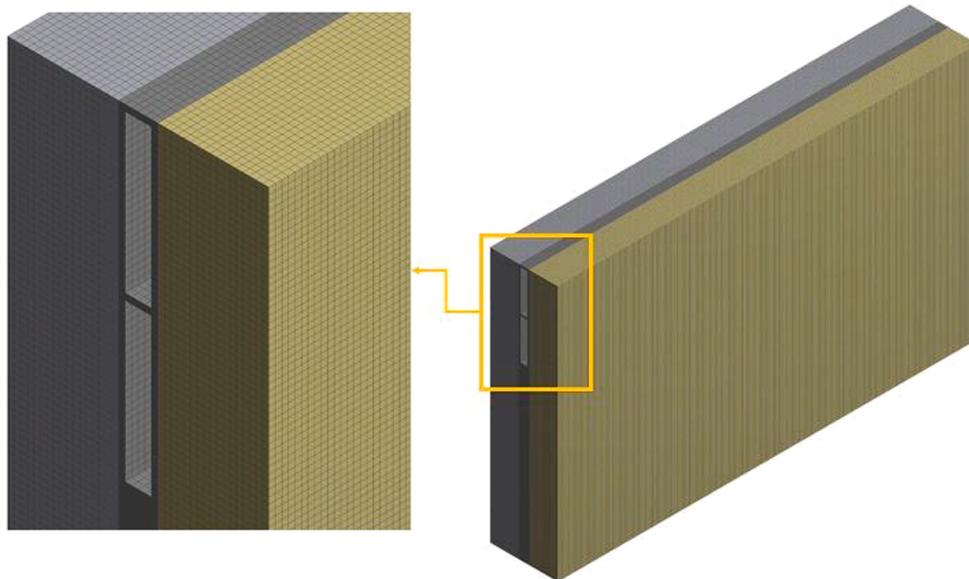
**Fig. 2.** Mesh model.

Table 5

Details of mesh.

Mesh Type	Mesh Sizing (m)	Nodes	Elements
Hex Dominated	5×10^{-4}	2,211,296	1,924,728

Table 6

Boundary conditions imposed to the coolant channels of LPC.

Mass Flow	T_{inlet}	Pressure Outlet	Mid Plane of LIB	Heat Source
$25 \times 10^{-3} \text{ (L s}^{-1}\text{)}$	30 °C	1 atm	Sym.	Eq. (10)

$$SOC(t) = 1 - \frac{It}{c_N} \quad (15)$$

Where c_N is the rated capacity of the cell (Ah). Hence, by combination of Eqs. (14), (15) and Table 4, the heat generation $q_v(t)$ can be calculated [33] which is utilized for the heat generation calculations.

Numerical solution

The CFD software, ANSYS-CFX version 17.2, a finite-volume-based package, is utilized to solve the governing equations numerically by thermal-fluid-solid coupling. Fig. 2 indicated the mesh type and model. Regarding the laminar flow regime a uniform grid is utilized and due to more accuracy and simplicity of the geometry a structured and hex dominated mesh type is used for both fluid and solid sections. Table 5 shows the details of the mesh for the simulations. To evaluate the numerical results, the grid independency tests are performed and the results are compared to the literature [33]. Throughout the simulation process, the heat transfer coefficient of the environment is considered $5 \text{ W m}^{-2} \text{ } ^\circ\text{C}^{-1}$, the ambient temperature is 30 °C [33], the time-step set as 1 s, the total time-steps is 400 s (the total discharge time for 9C-rate operation of the cells), and the iteration per time-step is 10 which is

appropriate according to the validation.

In addition, the grid-indecency in two different types of models, based on the convergence criteria, which is the RMS (root-mean-square) residual of 1×10^{-6} , is investigated. The boundary conditions, imposed to the coolant channels, are presented in Table 6. Fig. 3 shows the battery with all boundary conditions.

The behavior of flow, which is important to calculate the characteristic of the fluid flow can be explained by Reynolds number. Simulations represent that the Reynolds number is approximately below 325 in all cases. Therefore, the fluid flow regime is laminar.

Ribbed channels

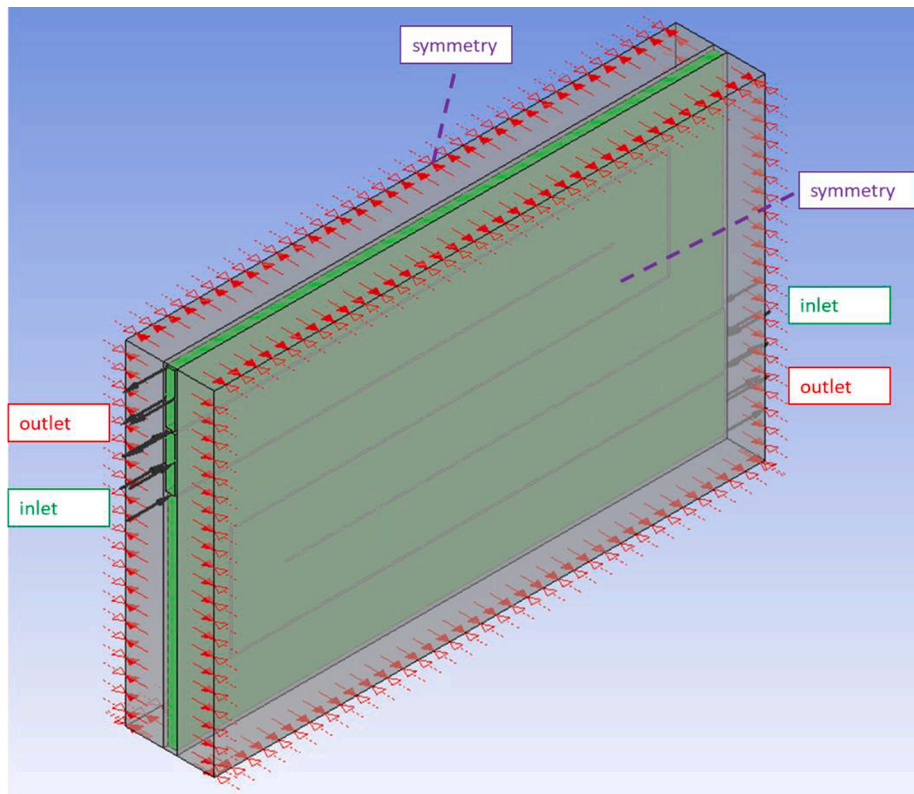
Specific types of longitudinal ribs created in the coolant channels. Fig. 4 shows the configuration of these ribs, which are designed in square form at various aspect ratios of W/D_H . In the optimization section, reduction of mass flowrate, enhancement of heat transfer crosses the battery cell, and enhancement of the battery hydrothermal cooling performance factor are considered as optimization parameters. Table 7 represents details of ribs. The boundary conditions, imposed on the coolant channels, are listed in Table 8.

Results and discussion

In this section, the validity of model, the heat transfer, the friction factor of ribbed channel, and the hydrothermal cooling performance are discussed. In addition, the effects of ribbed channels on the mass flowrate and pumping power and the optimization of ribbed channels in comparison with rib-less LCP are presented and analyzed.

Validation and grid independency

For the purpose of validation, the cell maximum temperatures in two different types of coolant channel geometries are compared with the

**Fig. 3.** Imposed boundary conditions.

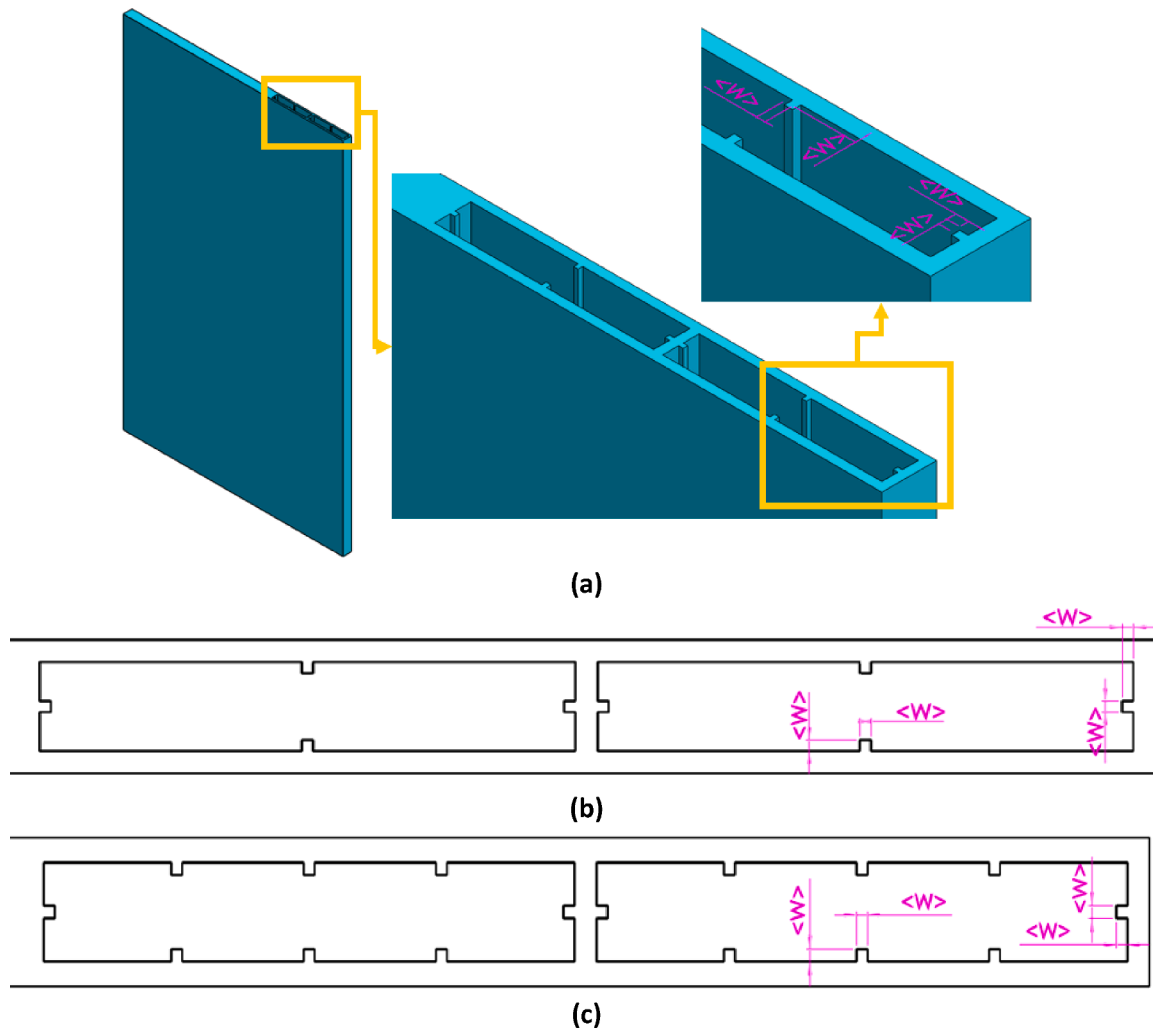


Fig. 4. Schematic of ribs. (a) Cooling channel ribs dimensions, (b) Cooling channel with 4 ribs, (c) Cooling channel with 8 ribs.

Table 7
Details of ribs in the coolant channels of LPC.

Case	Number of ribs	$\frac{W}{D_H}$
1	4	0.029155
2	4	0.036443
3	4	0.072886
4	8	0.072886

Table 8
Boundary conditions imposed to ribbed coolant channels of LPC.

P_{Tin} (Pa)	T_{inlet}	Pressure Outlet	Mid Plan of LIB	Heat Source
41.5114	30 °C	1 atm	Sym.	Eq. (10)

study of Sheng et al. [33]. Fig. 5(a) and Fig. 5(b) represent the maximum cell temperature at the coolant channel width of 4 mm under flowrate of $0.25 \times 10^{-3} \text{ L s}^{-1}$ and 12 mm with mass flowrate of $1 \times 10^{-3} \text{ L s}^{-1}$, respectively. The investigation focused on to show the effect of width of coolant channel and coolant flowrate simultaneously.

As both graphs show, there is a good agreement between the current simulation and the results reported by Sheng et al. [33]. As Fig. 5 shows that with increasing the mass flowrate by 400% and channel width by 300%, the maximum cell temperature reduced by approximately 4 K

after 400 time step. Based on the graph, the maximum deviation between current simulation and Sheng et al. [33] where the width coolant channel is 4 mm with mass flowrate of $0.25 \times 10^{-3} \text{ L s}^{-1}$ and 12 mm with mass flowrate $1 \times 10^{-3} \text{ L s}^{-1}$, are less than 3% and 4%, respectively. This deviation is deemed to be connected to the inaccuracy of the numerical simulations.

To shows that the obtained results are independent from the mesh, the grid independency study is performed for three different mesh structures including 0.94, 1.75, and 3.72 million grids, while the width of coolant channels are 4 mm. As Fig. 6 shows, the maximum deviation in the maximum cell temperature between 1.75 and 3.72 million grids is less than 0.08%, and between 0.94 and 1.75 million grids is less than 0.18%. Therefore, to reduce the computational cost in this research, the case with 1.75 million grids is considered for further investigations.

In the case of 12 mm width, the friction coefficient inside the coolant channels is 0.46, based on Eq. (8). Owing to the similar configuration of the two channels, the coefficient factor in the two coolant channels are equal. In this situation, the total wall heat flux on the battery (Q_0) is $1.07633 \times 10^8 \text{ W m}^{-2}$.

Effect of ribbed channels on friction factor

Fig. 7 illustrates the improvement of key performance factors in the studied scenarios. Fig. 7 (a) shows the proportion increase of friction factor in the ribbed channels relative to rib-less situation. It is observed that for all cases, based on the Eq. (8), the friction factor is enhanced by

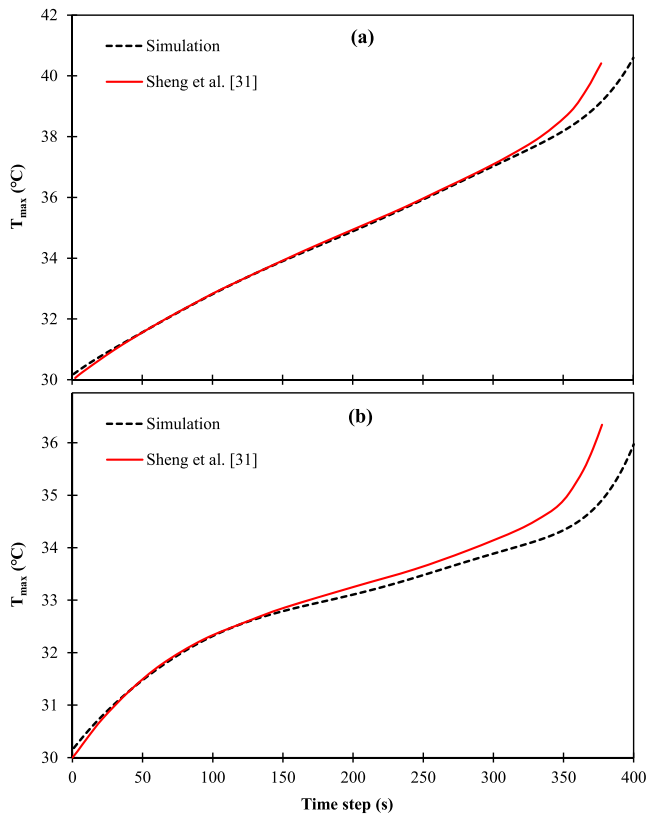


Fig. 5. Maximum cell temperature at the coolant channel width of (a) 4 mm and (b) 12 mm.

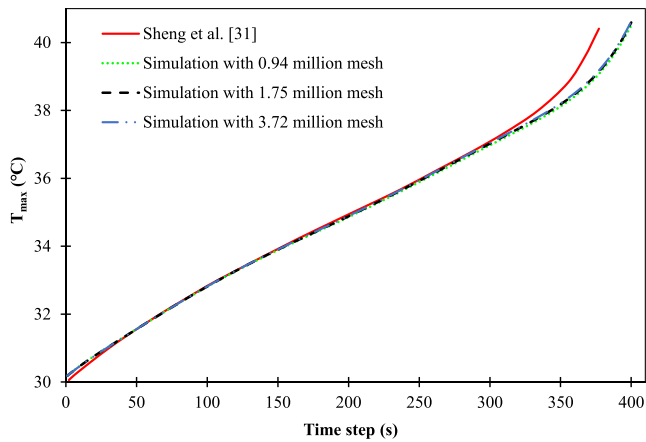


Fig. 6. Grid independency in the case where width of coolant channels is 4 mm.

increasing the number of ribs and increasing the ratio of W . According to Eq. (8), by reduction of Reynolds number, the friction factor is increased.

As Fig. 7 (a) displays, the maximum ratio of friction factor is 1.43, when the rib width is 0.25 mm and the number of ribs is 8. Clearly, the friction factor increases with the number of ribs and height of rib. Therefore, the friction factor ratio in case 4 is obviously more than the other cases. The enhancement of friction factor ratio for case 4 with 8 longitudinal ribs is approximately 19% compared with the other cases with 4 ribs, while the enhancement of friction factor ratio at the highest rib height is nearly 3%. This observation evidently indicates that the number of ribs is more effective on the friction factor than the height of rib.

Effect of ribbed channels on heat transfer

Increasing the heat transfer is one of the significant factors that effects the cooling of battery cells which can have a great effect on the life time of the battery. Fig. 7 (b) represents the ratio of heat transfer in the ribbed channels compared with the base case, i.e., the smooth coolant channels (without rib). According to the results, at low Reynolds numbers, the ratio of W of the embedded rib in the boundary layer do not have any effect on the maximum temperature of the battery cell. This is in agreement with the previous work [33], where the impact of coolant channel width on the maximum temperature of battery cells is reported to be minor. Based on Fig. 7 (d), with increasing the surface area of heat transfer, the maximum cell temperature is approximately remaining constant.

Based on the data presented in Fig. 7 (b), the heat transfer enhancement in case 1 and 2 are approximately similar and case 3 has the maximum ratio of heat transfer. In spite of increasing the heat transfer surface area in case 4 (compared to case 3), the heat transfer is nearly 27% lower in case 4 in comparison with case 3. This is deemed to be because of the mass flow reduction (Fig. 8 (a)) in case 4 which is more than case 3.

Effect of ribbed channels on hydrothermal performance

Since creating ribs in the coolant channels would have a huge impact on the friction factor and heat transfer, the effect of ribs on these parameters should be considered simultaneously. Consequently, the hydrothermal cooling factor defined to investigate this effect coincidently. According to Eq. (7), the thermal hydraulic performance calculated and for each case is depicted in Fig. 7 (c).

As Fig. 7 (c) shows, the maximum hydrothermal observed in the third case because in this case the heat transfer from the battery is in its highest level and friction factor is approximately minimum on the coolant channels of LCP.

Effect of ribbed channels on the mass flowrate and pumping power

The effects of ribs on the mass flowrate, pumping power, and ratio of power consumption is investigated in the last section. As Fig. 8 (a) illustrates, as the height and the number of ribs are increased, the mass flowrate of the coolant is reduced. In case 4, the required mass flowrate for each coolant channel is reduced by 16.02% in comparison with the rib-less channel.

The impact of ribs on the pumping power reduction for each ribbed channel is depicted in Fig. 8 (b). Based on the Eq. (9), the fluid velocity and the cross-sectional area are reduced for the ribbed channel, while simultaneously the pressure drop is constant. As a result, the pumping power reduced by up to 20%. According to the results and considering that the maximum temperature in the cells is kept constant compared to the rib-less channels, a smaller pump could be utilized which eventually would result in lower cost and energy consumption.

Power consumption of all the ribbed cooling channels in the LCP is shown in Fig. 8 (c). Based on Eq. (12) and Fig. 7 (a), with increasing the friction factor the power consumption is increased. It is clear that power consumption in case 1 and case 2 is approximately identical, and this trend is repeated for case 3 and case 4. It could, therefore, be concluded that increasing the ribs number has a minor effect on the power consumption.

Conclusions

The main goal of the current study was to optimize the hydrothermal cooling performance of a serpentine-shape channel with longitudinal ribs of LCP with multi channels. The effect of width and number of ribs on the temperature of LIB cell, the hydrothermal cooling performance, the mass flowrate reduction, the enhancement of heat transfer, and the

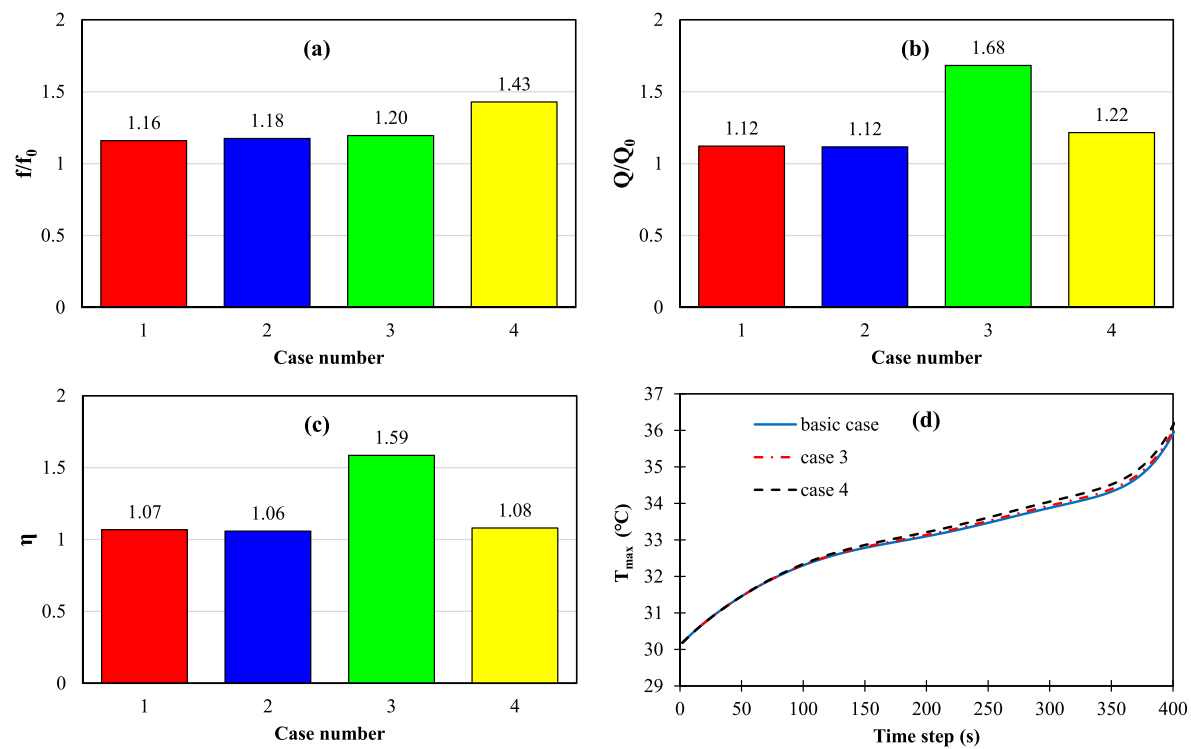


Fig. 7. Maximum cell temperature and performance comparison between 4 cases compared to the simple channel, (a) normalized friction factor, (b) the ratio of heat transfer, (c) the hydrothermal performance, and (d) maximum cell temperature.

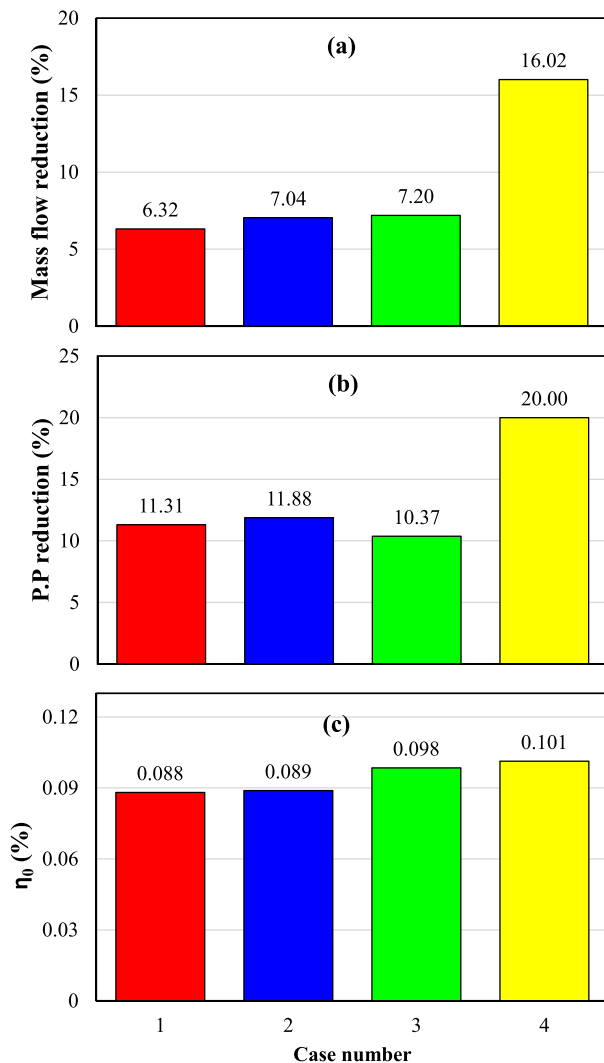


Fig. 8. Performance comparison between 4 cases compared to the simple channel, (a) The mass flowrate reduction, (b) The pumping power reduction, (c) The ratio of power consumption.

pumping power reduction were investigated. The results of this research could be significantly used in the lithium-ion battery industry to pave the way for producer of this precious field. In the circumstances of high temperature battery cells, this model can be effectively beneficial for increasing the battery life. Major findings of this study may be summarized as follows:

- The best hydrothermal cooling performance is increased by 59% in the third case with 4 ribs.
- The enhancement in the heat transfer is approximately 68% which occurred in the third case.
- The maximum mass flowrate reduction is in the 4th case at nearly 16%.
- The highest reduction in pumping power is about 20% for the 4th case.
- Thermal management performance of the LCP double ribbed channels is superior to rib-less channels.
- Four cases are designed in this research which can impressively decrease the pumping power as well as mass flowrate.
- Increasing the LCP heat transfer surface area has a minor effect on enhancing the cell maximum temperature, where in the superior case the maximum cell temperature is approximately constant.

- In terms of saving power and costs, case 4 is the optimum, and regarding increasing hydrothermal cooling performance, case 3 is performs best.

CRediT authorship contribution statement

Pourya Ashkboos: Methodology, Formal analysis, Software, Writing - original draft, Data curation. **Amin Yousefi:** Conceptualization, Formal analysis, Software, Writing - original draft, Data curation. **Ehsan Houshfar:** Conceptualization, Writing - review & editing, Supervision, Validation, Visualization.

Declaration of Competing Interest

The authors declare that they have no known competing financial interests or personal relationships that could have appeared to influence the work reported in this paper.

References

- [1] Akinyele DO, Rayudu RK. Review of energy storage technologies for sustainable power networks. *Sustain Energy Technol Assess* 2014;8:74–91. <https://doi.org/10.1016/j.seta.2014.07.004>.
- [2] Liu H, Wei Z, He W, Zhao J. Thermal issues about Li-ion batteries and recent progress in battery thermal management systems: A review. *Energy Convers Manage* 2017;150:304–30. <https://doi.org/10.1016/j.enconman.2017.08.016>.
- [3] Teng Ho, Ma Y, Yeow K, Thelliez M. An analysis of a Lithium-ion battery system with indirect air cooling and warm-up. *SAE Int J Passeng Cars Mech Syst* 2011;4(3):1343–57. <https://doi.org/10.4271/2011-01-2249>.
- [4] Zhao J, Rao Z, Huo Y, Liu X, Li Y. Thermal management of cylindrical power battery module for extending the life of new energy electric vehicles. *Appl Therm Eng* 2015;85:33–43. <https://doi.org/10.1016/j.applthermaleng.2015.04.012>.
- [5] Jouhara H, Khordehghah N, Serey N, Almahmoud S, Lester SP, Machen D, Wrobel L. Applications and thermal management of rechargeable batteries for industrial applications. *Energy* 2019;170:849–61. <https://doi.org/10.1016/j.energy.2018.12.218>.
- [6] Yu K, Yang Xi, Cheng Y, Li C. Thermal analysis and two-directional air flow thermal management for lithium-ion battery pack. *J Power Sources* 2014;270:193–200. <https://doi.org/10.1016/j.jpowsour.2014.07.086>.
- [7] Fan L, Khodadadi JM, Pesaran AA. A parametric study on thermal management of an air-cooled lithium-ion battery module for plug-in hybrid electric vehicles. *J Power Sources* 2013;238:301–12. <https://doi.org/10.1016/j.jpowsour.2013.03.050>.
- [8] Chen K, Wu W, Yuan F, Chen L, Wang S. Cooling efficiency improvement of air-cooled battery thermal management system through designing the flow pattern. *Energy* 2019;167:781–90. <https://doi.org/10.1016/j.energy.2018.11.011>.
- [9] Xun J, Liu R, Jiao K. Numerical and analytical modeling of lithium ion battery thermal behaviors with different cooling designs. *J Power Sources* 2013;233:47–61. <https://doi.org/10.1016/j.jpowsour.2013.01.095>.
- [10] Shah K, McKee C, Chalise D, Jain A. Experimental and numerical investigation of core cooling of Li-ion cells using heat pipes. *Energy* 2016;113:852–60. <https://doi.org/10.1016/j.energy.2016.07.076>.
- [11] Mohammadian SK, Zhang Y. Thermal management optimization of an air-cooled Li-ion battery module using pin-fin heat sinks for hybrid electric vehicles. *J Power Sources* 2015;273:431–9. <https://doi.org/10.1016/j.jpowsour.2014.09.110>.
- [12] Durmuş A, Durmuş A, Esen M. Investigation of heat transfer and pressure drop in a concentric heat exchanger with snail entrance. *Appl Therm Eng* 2002;22(3):321–32. [https://doi.org/10.1016/S1359-4311\(01\)00078-3](https://doi.org/10.1016/S1359-4311(01)00078-3).
- [13] Jiang G, Huang J, Liu M, Cao M. Experiment and simulation of thermal management for a tube-shell Li-ion battery pack with composite phase change material. *Appl Therm Eng* 2017;120:1–9. <https://doi.org/10.1016/j.applthermaleng.2017.03.107>.
- [14] Fathabadi H. High thermal performance lithium-ion battery pack including hybrid active-passive thermal management system for using in hybrid/electric vehicles. *Energy* 2014;70:529–38. <https://doi.org/10.1016/j.energy.2014.04.046>.
- [15] Chen J, Kang S, E J, Huang Z, Wei K, Zhang B, Zhu H, Deng Y, Zhang F, Liao G. Effects of different phase change material thermal management strategies on the cooling performance of the power lithium ion batteries: A review. *J Power Sources* 2019;442:227228. <https://doi.org/10.1016/j.jpowsour.2019.227228>.
- [16] Mehrabi-Kermani M, Houshfar E, Ashjaee M. A novel hybrid thermal management for Li-ion batteries using phase change materials embedded in copper foams combined with forced-air convection. *Int J Therm Sci* 2019;141:47–61. <https://doi.org/10.1016/j.ijthermalsci.2019.03.026>.
- [17] Kiani M, Ansari M, Arshadi AA, Houshfar E, Ashjaee M. Hybrid thermal management of lithium-ion batteries using nanofluid, metal foam, and phase change material: an integrated numerical-experimental approach. *J Therm Anal Calorim* 2020;141(5):1703–15. <https://doi.org/10.1007/s10973-020-09403-6>.
- [18] Mashayekhi M, Houshfar E, Ashjaee M. Development of hybrid cooling method with PCM and Al2O3 nanofluid in aluminium minichannels using heat source

- model of Li-ion batteries. *Appl Therm Eng* 2020;178:115543. <https://doi.org/10.1016/j.applthermaleng.2020.115543>.
- [19] Kiani M, Omiddezyani S, Houshfar E, Miremadi SR, Ashjaee M, Mahdavi Nejad A. Lithium-ion battery thermal management system with Al₂O₃/AgO/CuO nanofluids and phase change material. *Appl Therm Eng* 2020;180:115840. <https://doi.org/10.1016/j.applthermaleng.2020.115840>.
- [20] Safdari M, Ahmadi R, Sadeghzadeh S. Numerical investigation on PCM encapsulation shape used in the passive-active battery thermal management. *Energy* 2020;193:116840. <https://doi.org/10.1016/j.energy.2019.116840>.
- [21] Esen M. Thermal performance of a solar-aided latent heat store used for space heating by heat pump. *Sol Energy* 2000;69(1):15–25. [https://doi.org/10.1016/S0038-092X\(00\)00015-3](https://doi.org/10.1016/S0038-092X(00)00015-3).
- [22] Esen M, Durmuş A, Durmuş A. Geometric design of solar-aided latent heat store depending on various parameters and phase change materials. *Sol Energy* 1998;62(1):19–28. [https://doi.org/10.1016/S0038-092X\(97\)00104-7](https://doi.org/10.1016/S0038-092X(97)00104-7).
- [23] Esen M, Ayhan T. Development of a model compatible with solar assisted cylindrical energy storage tank and variation of stored energy with time for different phase change materials. *Energy Convers Manage* 1996;37(12):1775–85. [https://doi.org/10.1016/0196-8904\(96\)00035-0](https://doi.org/10.1016/0196-8904(96)00035-0).
- [24] Mohammadian SK, He Y-L, Zhang Y. Internal cooling of a lithium-ion battery using electrolyte as coolant through microchannels embedded inside the electrodes. *J Power Sources* 2015;293:458–66. <https://doi.org/10.1016/j.jpowsour.2015.05.055>.
- [25] Jilte RD, Kumar R, Ahmadi MH. Cooling performance of nanofluid submerged vs. nanofluid circulated battery thermal management systems. *J Cleaner Prod* 2019; 240:118131. <https://doi.org/10.1016/j.jclepro.2019.118131>.
- [26] Zhang YP, Yu XL, Feng QK, Zhang RT. Thermal performance study of integrated cold plate with power module. *Appl Therm Eng* 2009;29(17–18):3568–73. <https://doi.org/10.1016/j.applthermaleng.2009.06.013>.
- [27] Rao Z, Wang S, Wu M, Lin Z, Li F. Experimental investigation on thermal management of electric vehicle battery with heat pipe. *Energy Convers Manage* 2013;65:92–7. <https://doi.org/10.1016/j.enconman.2012.08.014>.
- [28] Wiriyaart S, Hommalee C, Sirikasemsuk S, Prurapark R, Naphon P. Thermal management system with nanofluids for electric vehicle battery cooling modules. *Case Stud Therm Eng* 2020;18:100583. <https://doi.org/10.1016/j.csite.2020.100583>.
- [29] Lyu Y, Siddique ARM, Majid SH, Biglarbegian M, Gadsden SA, Mahmud S. Electric vehicle battery thermal management system with thermoelectric cooling. *Energy Rep* 2019;5:822–7. <https://doi.org/10.1016/j.egy.2019.06.016>.
- [30] Cao J, Ling Z, Fang X, Zhang Z. Delayed liquid cooling strategy with phase change material to achieve high temperature uniformity of Li-ion battery under high-rate discharge. *J Power Sources* 2020;450:227673. <https://doi.org/10.1016/j.jpowsour.2019.227673>.
- [31] Cao J, Luo M, Fang X, Ling Z, Zhang Z. Liquid cooling with phase change materials for cylindrical Li-ion batteries: An experimental and numerical study. *Energy* 2020; 191:116565. <https://doi.org/10.1016/j.energy.2019.116565>.
- [32] Liu H-L, Shi H-b, Shen H, Xie G. The performance management of a Li-ion battery by using tree-like mini-channel heat sinks: Experimental and numerical optimization. *Energy* 2019;189:116150. <https://doi.org/10.1016/j.energy.2019.116150>.
- [33] Sheng L, Su L, Zhang H, Li K, Fang Y, Ye W, Fang Yu. Numerical investigation on a lithium ion battery thermal management utilizing a serpentine-channel liquid cooling plate exchanger. *Int J Heat Mass Transf* 2019;141:658–68. <https://doi.org/10.1016/j.ijheatmasstransfer.2019.07.033>.
- [34] Miranda D, Almeida AM, Lancers-Méndez S, Costa CM. Effect of the active material type and battery geometry on the thermal behavior of lithium-ion batteries. *Energy* 2019;185:1250–62. <https://doi.org/10.1016/j.energy.2019.07.099>.
- [35] Rehman MU, Siddique W, Haq I, Ali N, Farooqi Z. CFD analysis of the influence of guide ribs/vanes on the heat transfer enhancement of a trapezoidal channel. *Appl Therm Eng* 2016;102:570–85. <https://doi.org/10.1016/j.applthermaleng.2016.03.043>.
- [36] Valiantzas JD. Explicit power formula for the Darcy–Weisbach pipe flow equation: Application in optimal pipeline design. *J Irrig Drain Eng* 2008;134(4):454–61. [https://doi.org/10.1061/\(ASCE\)0733-9437\(2008\)134:4\(454\)](https://doi.org/10.1061/(ASCE)0733-9437(2008)134:4(454)).
- [37] Zhang S, Guo Xu, Dou X, Zhang X. A data-driven coulomb counting method for state of charge calibration and estimation of lithium-ion battery. *Sustain Energy Technol Assess* 2020;40:100752. <https://doi.org/10.1016/j.seta.2020.100752>.
- [38] Liu G, Ouyang M, Lu L, Li J, Han X. Analysis of the heat generation of lithium-ion battery during charging and discharging considering different influencing factors. *J Therm Anal Calorim* 2014;116(2):1001–10. <https://doi.org/10.1007/s10973-013-3599-9>.